Wearable speckle plethysmography (SPG) for characterizing microvascular flow and resistance

MICHAEL GHIJSEN,[1,2] TYLER B. RICE,[3] BRUCE YANG,[3] SEAN M. WHITE,[3] BRUCE J. TROMBERG[1,2,4,*]

[1]*Laser Microbeam and Medical Program, Beckman Laser Institute, 1002 Health Sciences Road, Irvine, CA 92612, USA*
[2]*Department of Biomedical Engineering, University of California, Irvine, CA 92697, USA*
[3]*Laser Associated Sciences Inc., 16 Foxglove Way, Irvine, CA 92612, USA*
[4]*Department of Surgery, University of California, Irvine Medical Center, Orange, CA 92868, USA*
*bjtrombe@uci.edu

Abstract: In this work we introduce a modified form of laser speckle imaging (LSI) referred to as affixed transmission speckle analysis (ATSA) that uses a single coherent light source to probe two physiological signals: one related to pulsatile vascular expansion (classically known as the photoplethysmographic (PPG) waveform) and one related to pulsatile vascular blood flow (named here the speckle plethysmographic (SPG) waveform). The PPG signal is determined by recording intensity fluctuations, and the SPG signal is determined via the LSI dynamic light scattering technique. These two co-registered signals are obtained by transilluminating a single digit (e.g. finger) which produces quasi-periodic waveforms derived from the cardiac cycle. Because PPG and SPG waveforms probe vascular expansion and flow, respectively, in cm-thick tissue, these complementary phenomena are offset in time and have rich dynamic features. We characterize the timing offset and harmonic content of the waveforms in 16 human subjects and demonstrate physiologic relevance for assessing microvascular flow and resistance.

References

1. J. Allen, "Photoplethysmography and its application in clinical physiological measurement," Physiol. Meas. **28**(3), R1–R39 (2007).
2. K. H. Shelley, "Photoplethysmography: beyond the calculation of arterial oxygen saturation and heart rate," Anesth. Analg. **105**(6), S31–S36 (2007).
3. A. B. Hertzman and W. C. Randall, "Regional differences in the basal and maximal rates of blood flow in the skin," J. Appl. Physiol. **1**(3), 234–241 (1948).
4. C. C. Brown, D. B. Giddon, and E. D. Dean, "Techniques of plethysmography," Psychophysiology **1**(3), 253–266 (1965).
5. J. G. Webster, *Design of pulse oximeters* (CRC Press, 1997).
6. K. Nakajima, T. Tamura, and H. Miike, "Monitoring of heart and respiratory rates by photoplethysmography using a digital filtering technique," Med. Eng. Phys. **18**(5), 365–372 (1996).
7. B. P. Imholz, W. Wieling, G. A. van Montfrans, and K. H. Wesseling, "Fifteen years experience with finger arterial pressure monitoring: assessment of the technology," Cardiovasc. Res. **38**(3), 605–616 (1998).
8. M. Azabji Kenfack, F. Lador, M. Licker, C. Moia, E. Tam, C. Capelli, D. Morel, and G. Ferretti, "Cardiac output by Modelflow® method from intra-arterial and fingertip pulse pressure profiles," Clin. Sci. **106**(4), 365–369 (2004).
9. B. Choi, N. M. Kang, and J. S. Nelson, "Laser speckle imaging for monitoring blood flow dynamics in the in vivo rodent dorsal skin fold model," Microvasc. Res. **68**(2), 143–146 (2004).
10. D. A. Boas and A. K. Dunn, "Laser speckle contrast imaging in biomedical optics," J. Biomed. Opt. **15**, 011109 (2010).
11. A. Fercher and J. Briers, "Flow visualization by means of single-exposure speckle photography," Opt. Commun. **37**(5), 326–330 (1981).

12. D. Briers, D. D. Duncan, E. Hirst, S. J. Kirkpatrick, M. Larsson, W. Steenbergen, T. Stromberg, and O. B. Thompson, "Laser speckle contrast imaging: theoretical and practical limitations," J. Biomed. Opt. **18**(6), 066018 (2013).

13. M. Draijer, E. Hondebrink, T. van Leeuwen, and W. Steenbergen, "Review of laser speckle contrast techniques for visualizing tissue perfusion," Lasers Med. Sci. **24**(4), 639–651 (2009).

14. D. D. Duncan and S. J. Kirkpatrick, "Can laser speckle flowmetry be made a quantitative tool?" J. Opt. Soc. Am. A **25**(8), 2088–2094 (2008).

15. A. Humeau-Heurtier, E. Guerreschi, P. Abraham, and G. Mahé, "Relevance of laser Doppler and laser speckle techniques for assessing vascular function: state of the art and future trends," IEEE Trans. Biomed. Eng. **60**(3), 659–666 (2013).

16. M. Ghijsen, B. Choi, A. J. Durkin, S. Gioux, and B. J. Tromberg, "Real-time wide-field metabolic imaging achieved through coherent spatial frequency domain imaging (cSFDI)," in *SPIE Photonics West - Advanced Biomedical and Clinical Diagnostic and Surgical Guidance Systems XIV*, (SPIE, 2016)

17. M. Ghijsen, G. R. Lentsch, S. Gioux, M. Brenner, A. J. Durkin, B. Choi, and B. J. Tromberg, "Quantitative real-time optical imaging of the tissue metabolic rate of oxygen consumption," J. Biomed. Opt. **23**(3), 1–12 (2018).

18. S. M. White, S. C. George, and B. Choi, "Automated computation of functional vascular density using laser speckle imaging in a rodent window chamber model," Microvasc. Res. **82**(1), 92–95 (2011).

19. C. Regan, S. M. White, B. Y. Yang, T. Takesh, J. Ho, C. Wink, P. Wilder-Smith, and B. Choi, "Design and evaluation of a miniature laser speckle imaging device to assess gingival health," J. Biomed. Opt. **21**(10), 104002 (2016).

20. C. Crouzet, R. H. Wilson, A. Bazrafkan, M. H. Farahabadi, D. Lee, J. Alcocer, B. J. Tromberg, B. Choi, and Y. Akbari, "Cerebral blood flow is decoupled from blood pressure and linked to EEG bursting after resuscitation from cardiac arrest," Biomed. Opt. Express **7**(11), 4660–4673 (2016).

21. M. A. Davis, L. Gagnon, D. A. Boas, and A. K. Dunn, "Sensitivity of laser speckle contrast imaging to flow perturbations in the cortex," Biomed. Opt. Express **7**(3), 759–775 (2016).

22. S. M. Daly and M. J. Leahy, "Advances in blood flow imaging," Advanced Biophotonics: Tissue Optical Sectioning, 321 (2016).

23. R. Bandyopadhyay, A. Gittings, S. Suh, P. Dixon, and D. Durian, "Speckle-visibility spectroscopy: A tool to study time-varying dynamics," Rev. Sci. Instrum. **76**(9), 093110 (2005).

24. B. Kruijt, H. S. de Bruijn, A. van der Ploeg-van den Heuvel, H. J. Sterenborg, and D. J. Robinson, "Laser speckle imaging of dynamic changes in flow during photodynamic therapy," Lasers Med. Sci. **21**(4), 208–212 (2006).

25. S. M. White, R. Hingorani, R. P. Arora, C. C. Hughes, S. C. George, and B. Choi, "Longitudinal in vivo imaging to assess blood flow and oxygenation in implantable engineered tissues," Tissue Eng. Part C Methods **18**(9), 697–709 (2012).

26. W. J. Moy, S. J. Patel, B. S. Lertsakdadet, R. P. Arora, K. M. Nielsen, K. M. Kelly, and B. Choi, "Preclinical in vivo evaluation of NPe6-mediated photodynamic therapy on normal vasculature," Lasers Surg. Med. **44**(2), 158–162 (2012).

27. A. Ponticorvo, R. Rowland, M. Baldado, D. Burmeister, R. Christy, N. Bernal, and A. Durkin, "Assessing the predictive capability of optical imaging techniques, Spatial Frequency Domain Imaging (SFDI) and Laser Speckle Imaging (LSI), to the gold standard of clinical assessment in a controlled animal model," in *Photonics in Dermatology and Plastic Surgery 2018*, (International Society for Optics and Photonics, 2018), 104670C.

28. R. Shi, M. Chen, V. V. Tuchin, and D. Zhu, "Accessing to arteriovenous blood flow dynamics response using combined laser speckle contrast imaging and skin optical clearing," Biomed. Opt. Express **6**(6), 1977–1989 (2015).

29. S. M. Jansen, D. M. de Bruin, D. J. Faber, I. J. G. G. Dobbe, E. Heeg, D. M. J. Milstein, S. D. Strackee, and T. G. van Leeuwen, "Applicability of quantitative optical imaging techniques for intraoperative perfusion diagnostics: a comparison of laser speckle contrast imaging, sidestream dark-field microscopy, and optical coherence tomography," J. Biomed. Opt. **22**(8), 1–9 (2017).

30. M. Gonzalez, N. Sevilla, J. Chue-Sang, and J. C. Ramella-Roman, "Quantitative analysis of a scar's pliability, perfusion and metrology," in *Optical Elastography and Tissue Biomechanics IV*, (International Society for Optics and Photonics, 2017), 100670R.

31. A. K. Dunn, H. Bolay, M. A. Moskowitz, and D. A. Boas, "Dynamic imaging of cerebral blood flow using laser speckle," J. Cereb. Blood Flow Metab. **21**(3), 195–201 (2001).

32. A. Mazhar, D. J. Cuccia, T. B. Rice, S. A. Carp, A. J. Durkin, D. A. Boas, B. Choi, and B. J. Tromberg, "Laser speckle imaging in the spatial frequency domain," Biomed. Opt. Express **2**(6), 1553–1563 (2011).

33. T. B. Rice, S. D. Konecky, A. Mazhar, D. J. Cuccia, A. J. Durkin, B. Choi, and B. J. Tromberg, "Quantitative determination of dynamical properties using coherent spatial frequency domain imaging," J. Opt. Soc. Am. A **28**(10), 2108–2114 (2011).

34. T. B. Rice, S. D. Konecky, C. Owen, B. Choi, and B. J. Tromberg, "Determination of the effect of source intensity profile on speckle contrast using coherent spatial frequency domain imaging," Biomed. Opt. Express **3**(6), 1340–1349 (2012).

35. A. B. Parthasarathy, W. J. Tom, A. Gopal, X. Zhang, and A. K. Dunn, "Robust flow measurement with multi-exposure speckle imaging," Opt. Express **16**(3), 1975–1989 (2008).

36. H. Qiu, Y. Zhou, Y. Gu, Q. Ang, S. Zhao, Y. Wang, J. Zeng, and N. Huang, "Monitoring microcirculation changes in port wine stains during vascular targeted photodynamic therapy by laser speckle imaging," Photochem. Photobiol. **88**(4), 978–984 (2012).
37. J. C. Ramirez-San-Juan, R. Ramos-García, I. Guizar-Iturbide, G. Martínez-Niconoff, and B. Choi, "Impact of velocity distribution assumption on simplified laser speckle imaging equation," Opt. Express **16**(5), 3197–3203 (2008).
38. C. Stoianovici, P. Wilder-Smith, and B. Choi, "Assessment of pulpal vitality using laser speckle imaging," Lasers Surg. Med. **43**(8), 833–837 (2011).
39. O. Yang and B. Choi, "Laser speckle imaging using a consumer-grade color camera," Opt. Lett. **37**(19), 3957–3959 (2012).
40. B. Yang, O. Yang, J. Guzman, P. Nguyen, C. Crouzet, K. E. Osann, K. M. Kelly, J. S. Nelson, and B. Choi, "Intraoperative, real-time monitoring of blood flow dynamics associated with laser surgery of port wine stain birthmarks," Lasers Surg. Med. **47**(6), 469–475 (2015).
41. K. Khaksari and S. J. Kirkpatrick, "Combined effects of scattering and absorption on laser speckle contrast imaging," J. Biomed. Opt. **21**(7), 076002 (2016).
42. M. J. Leahy, J. G. Enfield, N. T. Clancy, J. O'Doherty, P. McNamara, and G. E. Nilsson, "Biophotonic methods in microcirculation imaging," Med. Laser Appl. **22**(2), 105–126 (2007).
43. J. D. Briers, G. Richards, and X. W. He, "Capillary blood flow monitoring using laser speckle contrast analysis (LASCA)," J. Biomed. Opt. **4**(1), 164–175 (1999).
44. R. H. Wilson, C. Crouzet, M. Torabzadeh, A. Bazrafkan, M. H. Farahabadi, B. Jamasian, D. Donga, J. Alcocer, S. M. Zaher, B. Choi, Y. Akbari, and B. J. Tromberg, "High-speed spatial frequency domain imaging of rat cortex detects dynamic optical and physiological properties following cardiac arrest and resuscitation," Neurophotonics **4**(4), 045008 (2017).
45. J. Zötterman, R. Mirdell, S. Horsten, S. Farnebo, and E. Tesselaar, "Methodological concerns with laser speckle contrast imaging in clinical evaluation of microcirculation," PLoS One **12**(3), e0174703 (2017).
46. B. Lertsakdadet, B. Y. Yang, C. E. Dunn, A. Ponticorvo, C. Crouzet, N. Bernal, A. J. Durkin, and B. Choi, "Correcting for motion artifact in handheld laser speckle images," J. Biomed. Opt. **23**(3), 1–7 (2018).
47. T. Dragojević, D. Bronzi, H. M. Varma, C. P. Valdes, C. Castellvi, F. Villa, A. Tosi, C. Justicia, F. Zappa, and T. Durduran, "High-speed multi-exposure laser speckle contrast imaging with a single-photon counting camera," Biomed. Opt. Express **6**(8), 2865–2876 (2015).
48. S. C. Gnyawali, K. Blum, D. Pal, S. Ghatak, S. Khanna, S. Roy, and C. K. Sen, "Retooling laser speckle contrast analysis algorithm to enhance non-invasive high resolution laser speckle functional imaging of cutaneous microcirculation," Sci. Rep. **7**(1), 41048 (2017).
49. L. S. Costanzo, *Physiology* Third ed. (Saunders, 2006), p. 490.
50. W. B. Baker, A. B. Parthasarathy, D. R. Busch, R. C. Mesquita, J. H. Greenberg, and A. G. Yodh, "Modified Beer-Lambert law for blood flow," Biomed. Opt. Express **5**(11), 4053–4075 (2014).
51. B. Choi, J. C. Ramirez-San-Juan, J. Lotfi, and J. S. Nelson, "Linear response range characterization and in vivo application of laser speckle imaging of blood flow dynamics," J. Biomed. Opt. **11**, 041129 (2006).
52. J. D. Briers, "Laser Doppler, speckle and related techniques for blood perfusion mapping and imaging," Physiol. Meas. **22**(4), R35–R66 (2001).
53. S. L. Jacques, "Optical properties of biological tissues: a review," Phys. Med. Biol. **58**(11), R37–R61 (2013).
54. F. Ayers, A. Grant, D. Kuo, D. J. Cuccia, and A. J. Durkin, "Fabrication and characterization of silicone-based tissue phantoms with tunable optical properties in the visible and near infrared domain," in *Biomedical Optics (BiOS) 2008*, (International Society for Optics and Photonics, 2008), 687007.
55. S. N. Doshi, K. K. Naka, N. Payne, C. J. Jones, M. Ashton, M. J. Lewis, and J. Goodfellow, "Flow-mediated dilatation following wrist and upper arm occlusion in humans: the contribution of nitric oxide," Clin. Sci. **101**(6), 629–635 (2001).
56. D. H. Thijssen, M. W. Bleeker, P. Smits, and M. T. Hopman, "Reproducibility of blood flow and post-occlusive reactive hyperaemia as measured by venous occlusion plethysmography," Clin. Sci. **108**(2), 151–157 (2005).
57. S. Verma, M. R. Buchanan, and T. J. Anderson, "Endothelial function testing as a biomarker of vascular disease," Circulation **108**(17), 2054–2059 (2003).
58. M. S. Menkes, K. A. Matthews, D. S. Krantz, U. Lundberg, L. A. Mead, B. Qaqish, K.-Y. Liang, C. B. Thomas, and T. A. Pearson, "Cardiovascular reactivity to the cold pressor test as a predictor of hypertension," Hypertension **14**(5), 524–530 (1989).
59. D. E. Warburton, M. J. Haykowsky, H. A. Quinney, D. P. Humen, and K. K. Teo, "Reliability and validity of measures of cardiac output during incremental to maximal aerobic exercise. Part II: Novel techniques and new advances," Sports Med. **27**(4), 241–260 (1999).
60. A. Burton, "The range and variability of the blood flow in the human fingers and the vasomotor regulation of body temperature," American Journal of Physiology–Legacy Content **127**(3), 437–453 (1939).
61. H. Barcroft and O. Edholm, "Temperature and blood flow in the human forearm," J. Physiol. **104**(4), 366–376 (1946).
62. N. A. Lassen, J. Lindbjerg, and O. Munck, "Measurement of blood-flow through skeletal muscle by intramuscular injection of Xenon-133," Lancet **283**(7335), 686–689 (1964).
63. R. Morecraft, W. F. Blair, T. D. Brown, and R. H. Gable, "Acute effects of smoking on digital artery blood flow in humans," J. Hand Surg. Am. **19**(1), 1–7 (1994).

64. W. B. Murray and P. A. Foster, "The peripheral pulse wave: information overlooked," J. Clin. Monit. **12**(5), 365–377 (1996).
65. G. Mardirossian and R. E. Schneider, "Limitations of pulse oximetry," Anesth. Prog. **39**(6), 194–196 (1992).
66. M. J. Hayes and P. R. Smith, "A new method for pulse oximetry possessing inherent insensitivity to artifact," IEEE Trans. Biomed. Eng. **48**(4), 452–461 (2001).
67. J. Allen and A. Murray, "Age-related changes in the characteristics of the photoplethysmographic pulse shape at various body sites," Physiol. Meas. **24**(2), 297–307 (2003).
68. E. Chung, G. Chen, B. Alexander, and M. Cannesson, "Non-invasive continuous blood pressure monitoring: a review of current applications," Front. Med. **7**(1), 91–101 (2013).

1. Introduction

Photoplethysmography is a well-established technique in which light is transmitted through tissue in order to interrogate vascular fluctuations caused by the cardiac cycle [1, 2]. These fluctuations are due to volumetric expansion of blood caused by variations in pressure which ultimately modulate the attenuation of transmitted light [3, 4]. Analyzing the Photoplethysmographic (PPG) cardiac waveforms has been used extensively as a means for hemodynamic characterization [5–8]. One successful example is pulse oximetry in which the AC components of the PPG waveform at multiple optical wavelengths are used to calculate arterial hemoglobin oxygen saturation [5]. However, PPG has failed to achieve wide-spread clinical adoption in other important applications such as continuous noninvasive arterial pressure, arterial stiffness characterization, and noninvasive cardiac output monitoring [7, 8]. One reason for this is the tendency of the PPG waveform to deteriorate in situations of low peripheral blood flow such as hypovolemia or thermoregulatory vasoconstriction [1]. In addition, PPG may lack sufficient information content to properly characterize the cardiovascular system.

Laser Speckle Imaging (LSI) is a non-contact imaging modality capable of measuring relative perfusion by utilizing a coherent light source and a CMOS or CCD detector [9–22]. Scattered coherent light generates a speckle interference pattern on the detector which can be analyzed computationally to measure the speed of the light-scattering particles [23–30]. Relative blood flow can be determined with this image by measuring the fluctuations in the speckle pattern and the overall blurring of the individual speckles [31–42]. This technique is typically performed in reflectance geometry with the light source and the camera on the same side of the sample. In this configuration the depth penetrance is typically on the order of 500 – 1000 microns [43, 44]. Although LSI is very useful for measuring relative perfusion in a given area of tissue, it requires an optical system that can be cumbersome in a clinical environment and is susceptible to motion artifacts [45–48].

Affixed Transmission Speckle Analysis (ATSA) addresses some of the shortcomings of LSI by utilizing transmission geometry. One format that ATSA can be performed in is a miniaturized form factor attached to a digit, similar to a conventional pulse-oximeter. In this setup, the highly diffuse photons probe the full thickness of tissue and provide a high-SNR signal that can be used to determine average flow. The clip-on design further improves signal quality by reducing motion artifacts. Importantly, ATSA is also capable of detecting fluctuations in laser coherence due to the cardiac cycle. We refer to the methodology of obtaining this signal as speckle plethysmography (SPG). Additionally, this instrument is sensitive to the PPG waveform; volumetric vessel changes associated with cardiac pulsatility modulate light intensity. Thus, ATSA ultimately provides simultaneous, co-registered SPG-PPG output.

In this work we introduce ATSA and validate its sensitivity to flow in finger-like tissue phantoms. In a series of human volunteers, we demonstrate the process by which the SPG and PPG waveforms can be extracted from the same raw data and provide a physiological mechanism for the origin of both signals. We show that SPG and PPG signals are offset in time, and evaluate the harmonic content of the dynamic, temporally varying SPG waveform. Time-delay and frequency content signal decomposition strategies are applied to *in vivo* measurements in 16 volunteers and used to evaluate correlations between SPG-PPG

parameters and age. We assess sensitivity to vascular tone (the degree of constriction or resistance in blood vessels [49]) by measuring four subjects undergoing two controlled physiologic perturbations: exercise and cold pressor challenges. To evaluate repeatability in this same context, a single patient was followed for seven measurements for each physiological perturbation. Our results clearly highlight the sensitivity of the time-delay and waveform features in response to these challenges, and underscore how this new approach can be used to assess important vascular parameters: microvascular perfusion, vascular tone and vessel resistance. In a broader context, these fundamental parameters are critical to understanding derived metrics such as blood pressure, cardiac output and fluid status.

2. Materials and methods

2.1 Instrumental assembly

The ATSA instrument lends itself particularly well to being incorporated in a compact finger-clip. We obtained a commercially available ATSA device (Flowmet, LAS, Inc., Irvine, CA). This instrument takes advantage of highly diffuse speckle signals that have penetrated the skin at least several mm. The light source consists of a 785 nm laser diode while the detector consists of a 752-pixel x 480-pixel CMOS array. An aperture is placed in front of the detector to selectively filter the coherent signal from ambient light. The source and detector are placed opposite one another in a form factor practically identical to a commercially available pulse-oximeter.

To clarify nomenclature, ATSA refers to the specific instrument setup used in this manuscript, while SPG refers the process of obtaining pulsatile speckle fluctuations due to the cardiac cycle. The signal directly recovered using SPG will be referred to as the SPG waveform or SPG signal, keeping with the same convention as PPG.

2.2 Theory

Figure 1 shows how the SPG and PPG signals are extracted from raw data. Within the ATSA device there is a 785 nm laser diode placed opposite to a 752-pixel x 480-pixel CMOS camera. The camera acquires images of the diffuse speckle interference pattern at approximately 200 frames per second. On a frame-by-frame basis, a 7-pixel x 7-pixel sliding window filter is used to extract the mean intensity $<I>$ and the standard deviation $<\sigma>$ of the raw images. The single black and red squares underneath the $<I>$ and $<\sigma>$ signify that the 7-pixel by 7-pixel sliding window array is condensed into single values. This data is used to construct the average intensity and the speckle contrast (K) matrices. K is the ratio of the standard deviation to the mean intensity. At this point, the average intensity array is used produce the PPG signal array using the following PPG equation: $\Psi_{PPG} = 1/ln(<I>)$, where Ψ_{PPG} is the PPG signal [31, 50]. The average of the entire PPG array yields to the single PPG signal timepoint. At the same time the speckle contrast is used to produce the SPG signal array using the equation shown in Fig. 1. This equation has been validated experimentally to produce a metric that is linear with respect to volumetric flow [51]. Finally, this array is averaged to produce a single SPG signal timepoint. This process is repeated for each frame to construct the SPG and PPG time-series – all from the same raw data.
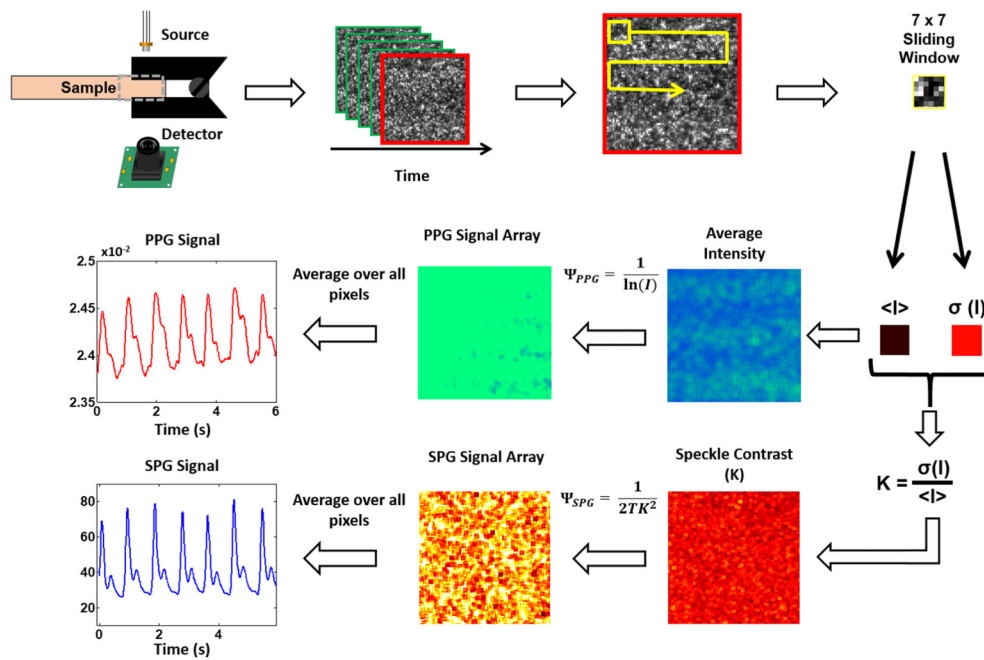
Fig. 1. ATSA signal processing diagram. The schematic shows the core algorithmic steps from acquisition of raw data to the final SPG and PPG waveforms.

Figure 2 demonstrates how the SPG and PPG signals are related to vascular physiology. Figure 2(a) depicts how the sample, typically a digit on the subject's hands or feet, is placed within the finger clip such that it falls between the source and detector. As demonstrated in Fig. 2(b), light from the coherent source enters the tissue and is dispersed randomly by a combination of static and dynamic scatterers [52, 53]. Static scatterers are comprised of matrix materials (e.g. collagen) and membranes belonging to stationary cells and organelles [53]. Dynamic scatterers consist of the membranes belonging to moving red blood cells [52]. Light passing through the tissue is also attenuated by absorbers contained in the tissue; the most important of these is hemoglobin, the oxygen-transporting molecule confined in the cytoplasm of red blood cells [53]. Dynamic scattering modulates the speckle pattern incident on the CMOS detector, producing the SPG signal (Fig. 2(c)). Likewise, attenuation due to absorbers modulates light intensity, producing the PPG signal (Fig. 2(d)). The pulsatile nature of blood pressure within the arteries and arterioles is well-established, but this pulsatility wanes downstream in the capillary and venous plexuses [49]. Therefore, it is likely that pulsatility in both attenuation and coherence originates from the arterial side of the vasculature. Pulsatility in the SPG waveform is due to variation in dynamic scattering related to volumetric flow, whereas pulsatility in the PPG waveform is due to variation in the concentration of absorbers caused by vessel expansion [1]. Thus, the SPG and PPG waveforms embody two pulsatile signals originating from different electromagnetic properties and are related to distinct physiological processes.

The SPG waveform in the black dotted box on the right side of Fig. 2(c) contains arrows indicating components of the cardiac cycle referenced later. The thick red arrow points to the systolic upstroke in which ejection of blood through the aorta rapidly increases. The black dotted arrow shows the systolic peak, the apex of blood flow. Lastly, the solid black arrow designates a secondary reflection, a reverberation caused by refractive index mismatches at vessel branch-points.
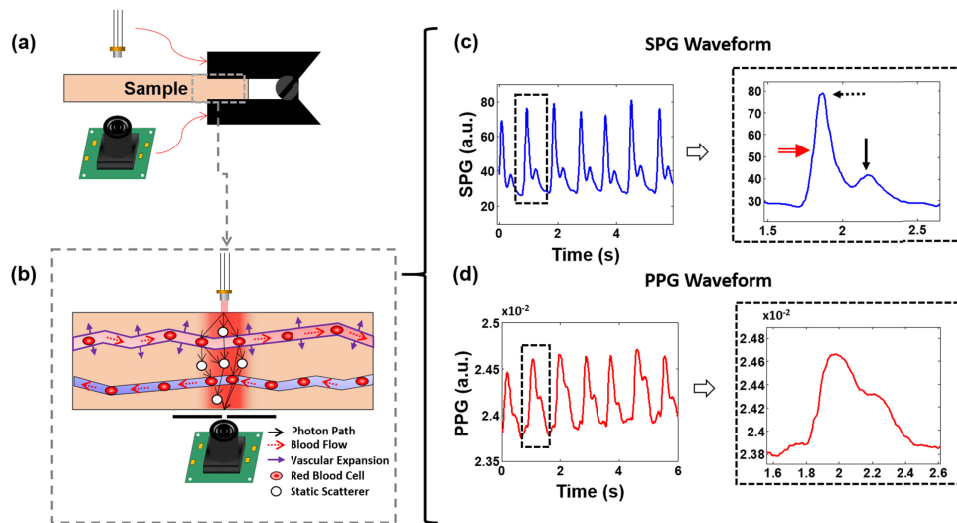
Fig. 2. ATSA Instrument Description. (a) Orientation of the core hardware components, casing and tissue sample. (b) Physiological origin of the SPG and PPG signals. (c) SPG waveform example. (d) PPG waveform example

2.3 Data processing procedures

In this work we present two SPG-PPG processing methodologies. Figure 3 graphically shows how time-delay (TD) is calculated. The systolic peaks (red and green asterisks) are located on a beat-by-beat basis for both the SPG and PPG signals. This is done automatically using a global peak-finding algorithm based on minimized slopes and is available in many computational software packages. TD is then calculated by subtracting the SPG peak time from the PPG peak time for every heartbeat in the data set. The average is then taken from at least 120 heartbeats.
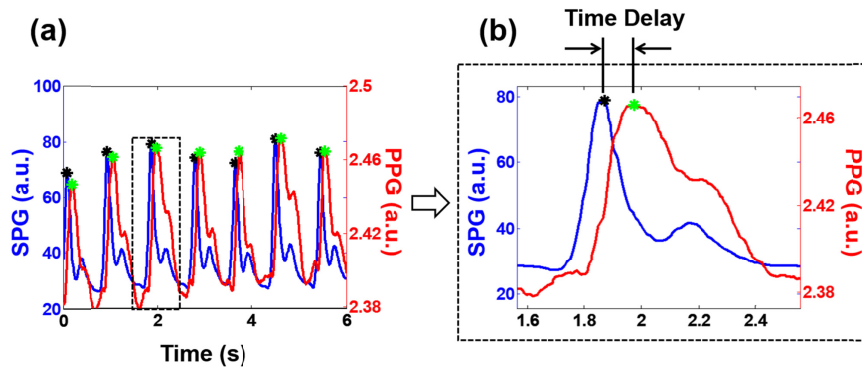

Fig. 3. TD Algorithm. (a) The SPG and PPG signals in blue and red, respectively. The black dotted rectangle demarcates the single pulse in Fig. 3(b). (b) Close-up of a single cardiac cycle. The two parallel lines flanked by the inward pointing black arrows visually depict the time delay. In both panels, the black asterisks mark the systolic peaks of the SPG waveform and the green asterisks mark the systolic peaks of the PPG waveform.

Figure 4 shows the SPG harmonic content extraction process. In this procedure, a single heartbeat is isolated from the SPG time-series. The pulse is Fourier transformed to produce a

harmonic spectrum. This is a spectrum of discrete peaks corresponding to the fundamental frequency (heart rate) and subsequent harmonics of the waveform. Finally, the height of each discrete peak is determined and used to produce harmonic ratios. These ratios are stored in an array and then the process is repeated for the next heartbeat in the time-series. An average is taken to produce a single measurement for each ratio. In this work we focus our analysis on the third harmonic ratio (H3 / H1) as shown in Fig. 4.
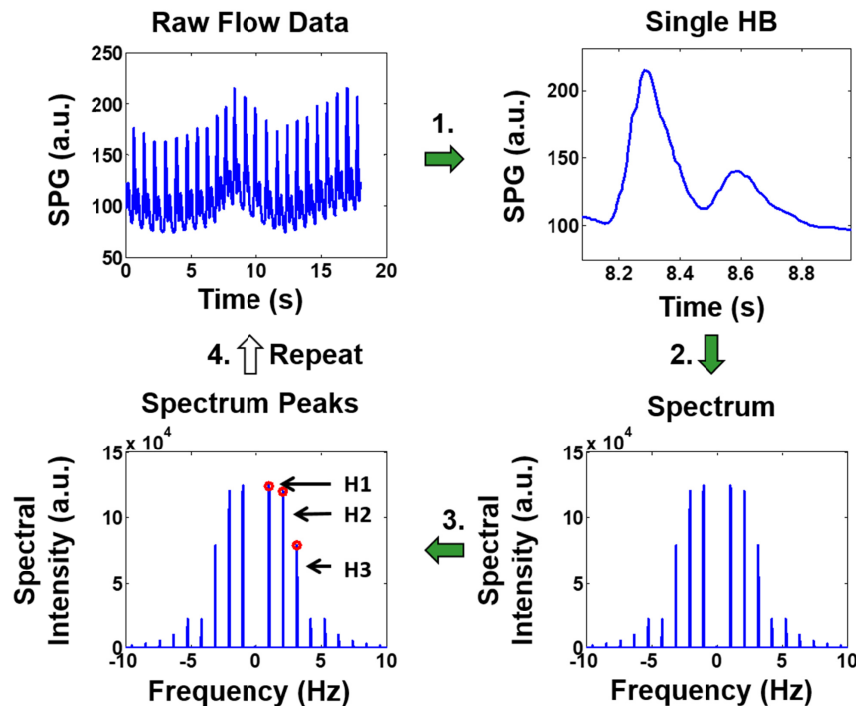
Fig. 4. Time Frequency Analysis algorithm. The top left shows a raw SPG tracing from which (1) a single cardiac waveform is extracted. (2) The FFT of the waveform is computed to yield the frequency spectrum, consisting of distinct harmonic peaks. (3) The height of each harmonic is used to calculate harmonic ratios, discrete values stored for each cardiac cycle. (4) The algorithm repeats for the next cardiac cycle, accumulating harmonic ratios into a distribution that can be visualized with a histogram or used to compute a mean.

2.4 Phantom validation

A controlled preliminary validation experiment was performed to test linearity of ATSA in the physiological flow regimes of interest. A finger analog was synthesized using silicone rubber and impregnated with single wound transparent tube (< 1 mm inner diameter) designed to mimic small arteries and arterioles within a digit. The tube network was connected in series to a syringe pump (Pump Systems, Inc.). Optical scattering and absorption coefficients of the silicone rubber were adjusted with titanium dioxide and nigrosin powder to achieve an absorption coefficient of 0.02 mm^{-1} and a reduced scattering coefficient of 1.0 mm^{-1}, values which are comparable to tissue at 785 nm [54]. Defibrinated sheep blood (Quadfive Materials Bio, Inc.) was pumped through the phantom at known volumetric flow rates. The flow was increased once per second in intervals of 0.2 mL/min up to a maximum of 20 mL/min, approximating the physiological range. The ATSA flow metric was compared to the flow control over this range.

2.5 Physiological challenges

2.5.1 Post-occlusive reactive hyperemia

The post-occlusive reactive hyperemia (PORH) challenge consisted of occluding a subject's upper arm for three minutes using a pneumatic cuff pressurized to 215 mmHg [55, 56]. The occlusion leads to a buildup of metabolic byproducts which vasodilate the arm causing a significantly increased blood flow when the cuff is depressurized. The state of relatively increased blood flow in PORH amplifies the PPG waveform. It should be noted that PORH was not used for its usual intended purpose of comparing the hyperemic state to baseline measurements for measuring endothelial function [57]. In this work, 16 subjects aged 23 to 81 (11 females and five males) were each measured with ATSA using a protocol consisting of a 5-minute baseline, 3-minute occlusion, and 5-minute post-release period. Intervals within the baseline and post-release periods were analyzed to obtain the physiological parameters discussed above.

2.5.2 Cold pressor challenge

The cold pressor challenge consisted of a subject submerging one hand in ice water for 30 to 90 seconds inducing peripheral vasoconstriction along with a slight increase in heart rate and blood pressure [58]. In this work, the ATSA device was attached to the subject's left index finger while a baseline measurement was acquired for two to three minutes. At this point the subject inserted his contralateral hand (right hand in this case) into ice water for as long as tolerable – usually 30 to 90 seconds – while data continued to be acquired on the non-submerged hand. This data was processed to calculate TD. In order to assess repeatability, this process was repeated on one subject seven times. In order to assess the effects in general, this test was performed on four subjects aged 25 – 35; there were three males and one female. The study was carried out under a UC Irvine IRB approved protocol and informed consent was obtained (HS #2004-3626).

2.5.3 Exercise challenge

The exercise challenge consisted of 10 minutes of cardiovascular exercise on a stationary bicycle. The left index finger was measured with the ATSA for two minutes before and two minutes following the challenge. Cardiovascular exercise is known to decrease peripheral vasoconstriction especially in the superficial vascular beds [59]. It also increases blood pressure and cardiac output by increasing the heartrate and stroke volume. The decreased peripheral vasoconstriction is required to vent excess heat and the increased cardiac output is necessary to supply working muscle with oxygen and nutrients needed for heightened metabolic activity. Like the cold pressor challenge, repeatability was assessed with seven repeat measurements on one subject, and general effect was assessed with one measurement on four subjects.

3. Results

3.1 Validation

Figure 5 shows an illustration of the in vitro test setup and a plot of ATSA recordings for a range of volumetric blood flow. The ATSA instrument depicted in Fig. 5(a) produced flow index $1/(2TK^2)$ values between (1-150) over the volumetric flow range (0-20) mL/min. The relationship between measured flow index and known volumetric flow is plotted in Fig. 5(b), where the ATSA instrument shows significant linearity ($R^2 = 0.98$). For each 10-second measurement, the standard deviation of the flow index was less 0.5%. The specified flow range encompasses values observed in prior literature and in healthy subjects [60–63]. This suggests the ATSA output is linearly proportional to the volumetric flow rate in the physiological range of interest.
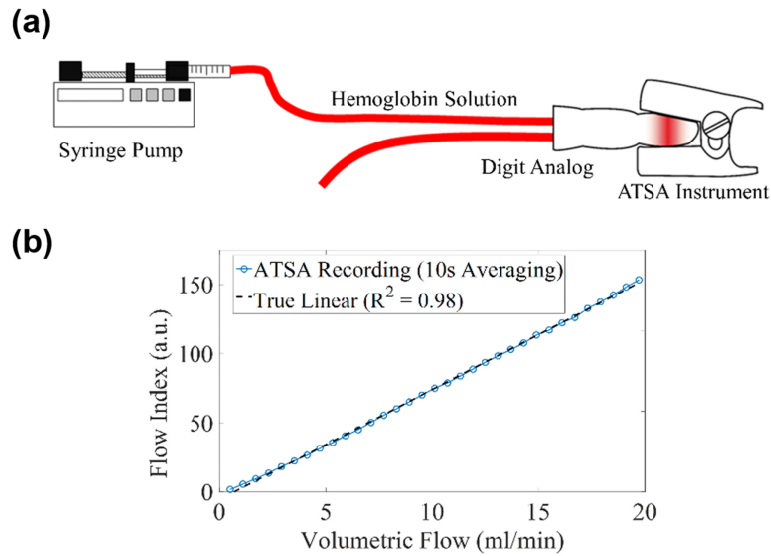
(a)

(b)

Fig. 5. In-vitro validation test setup. (a) A syringe pump pushes a hemoglobin solution through a Digit Analog with a clipped on ATSA instrument. (b) Measured flow index in arbitrary units plotted against volumetric flow in ml per minute. The blue circles show ATSA recordings averaged over 10 seconds while the dotted black line shows a linear fit with an R^2 coefficient of 0.98.

3.2 Relative SPG and PPG signal quality

Figure 6 shows the SPG and PPG waveforms during high and low perfusion. Exercise and cold pressor challenges were used to reproduce high and low blood flow, respectively. Figure 6(a) shows the SPG and PPG waveforms during exercise. Both signals have a high signal-to-noise ratio (SNR) as exhibited by the prominent and undistorted systolic peaks. Notably, the trough of the PPG signal contains trace amounts of noise. Figure 6(b) shows both signals during a cold pressor challenge. The PPG waveform in this condition shows significantly decreased SNR while the SPG signal remains robust.

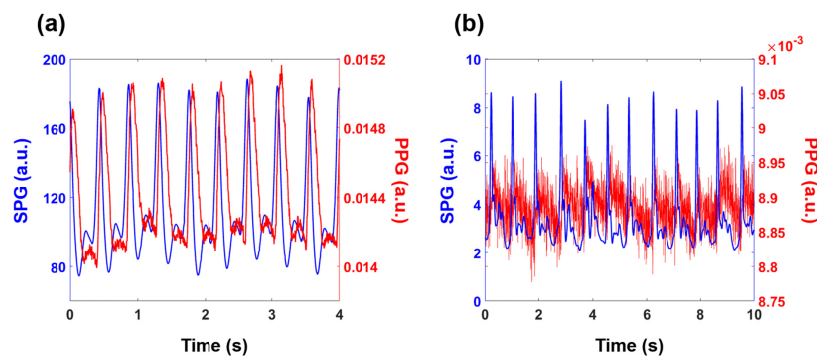**(a)**   **(b)**

Fig. 6. Comparison of distortion of SPG and PPG signals. (a) Dual-axis plot of the SPG and PPG waveforms during exercise. (b) Dual-axis plot the SPG and PPG waveforms during a cold pressor challenge. In both graphs, SPG signal is blue and PPG signal is red.

3.3 Change in TD and harmonic content observed with age

Figure 7 shows the TD results for two subjects calculated from the 300-second interval directly following the arterial occlusion release (see *post-occlusive reactive hyperemia* in the methods section). Subject A is a 71-year-old female with known cardiovascular risk factors including a history of smoking, hyperlipidemia, hypertension and type-2 diabetes. Subject B is a 23-year-old male with no known significant cardiovascular risk. These two subjects were chosen as an archetypal example of how TD can vary among patients. Figure 7(a) shows a dual-axis plot of a 4-second SPG (blue) and PPG (red) signal interval for Subject A, while Fig. 7(b) shows the same dual-axis plot for Subject B. The black asterisks show the local maxima of the SPG waveform and the green asterisks show the local maxima of the PPG waveform. Notably, the PPG signal of Subject A is broader than that of Subject B, who has much more pronounced signal peaks. Additionally, Subject B's PPG waveform more closely resembles the SPG waveform. These signal characteristics appear to contribute to the longer TD of Subject A. Figure 7(c) presents a histogram distribution of TD for both subjects. Each distribution was derived from approximately 300 heartbeats. This histogram demonstrates that Subject A has both a greater TD and a wider distribution.
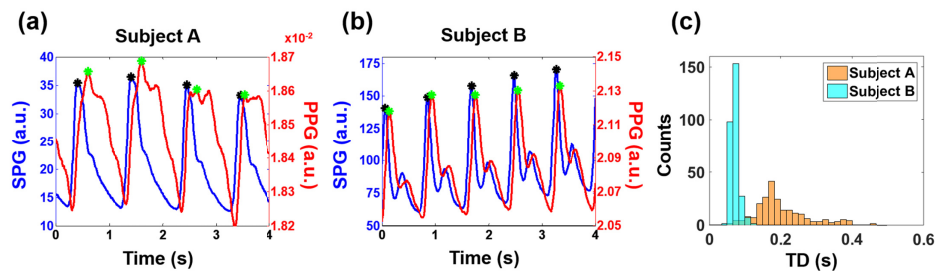

Fig. 7. Two Subject Comparison of TD. (a) Dual-axis plot of the SPG and PPG waveforms marked for Subject A. (b) Dual axis plots of the SPG and PPG waveforms for Subject B. In both Fig. 6(a) and (b), SPG and PPG signals are blue and red, respectively. The SPG and PPG signal peaks are highlighted with black and green asterisks, respectively. (c) Histogram distribution of TD calculated for both subjects. The histogram values were extracted from approximately 300 pulses each.

Figure 8 shows the harmonic content results for the same two subjects calculated from the 300-second time interval following the release of the arterial cuff occlusion. The third harmonic ratio (THR), which is the ratio of the third harmonic to the first harmonic (fundamental), was used in this example. To reiterate, this demonstration is meant as an archetypal example of the variation among patients with differing age and cardiovascular risk. Figure 8(a) and 8(c) present the SPG waveforms extracted from Subject A and Subject B, respectively. For reference, the systolic upshot and systolic peak are labeled in Fig. 8(a), and the secondary reflection is labeled in Fig. 8(c). Qualitatively, Subject B contains more structure and harmonic content than Subject A as evidenced by the secondary reflection. The Fourier transforms of the SPG waveforms are shown in Fig. 8(b) and 8(d) with the first and third harmonics labeled H1 and H3, respectively. THR consists of the ratio of the third peak to the first peak (H3 / H1). The histogram in Fig. 8(e) shows the THR distributions for both subjects, demonstrating that Subject B has a higher mean THR and a broader distribution than Subject A. In other words, the older subject (Subject A) had less harmonic content as exhibited by the smaller mean THC, and a more repetitive structure as exhibited by the smaller variation in the distribution.
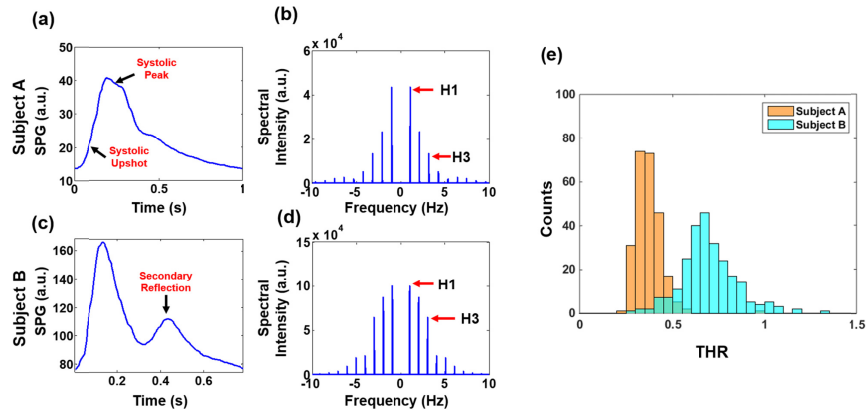
Fig. 8. Time Frequency Analysis Comparison. (a) Single cardiac cycle extracted from the raw flow data of Subject A. (b) Frequency spectrum computed for Subject A's waveform wherein H1 and H3 demarcate the first (fundamental) and third harmonic, respectively. (c) Single cardiac cycle taken from Subject B. (d) Frequency spectrum computed for Subject B's waveform. As in Fig. 8(b), H1 and H3 point to the first and third harmonic. (e) Histogram distribution of THR for Subject A (orange) and Subject B (turquoise). The distributions for each subject were extracted from approximately 300 heartbeats.

Overall, Fig. 7 and Fig. 8 demonstrate major differences between two archetypal extremes. The young healthy subject has a relatively short TD and a relatively high THR, while the opposite is true of the older patient with significant cardiovascular risk. Looking at a wider spectrum of subjects provides a better understanding of the parameters' dependence on vessel health.

Figure 9 presents regression analysis of TD and THR onto subject age. The solid red lines indicate the best linear fit, the dotted red lines show the 95% confidence intervals, and the blue tick-marks are individual subject data. All data points are calculated from the interval following the release of an arterial cuff occlusion as described in the methods section. The adjusted R^2 values for TD vs. age and THR vs. age were 0.686 and 0.538 respectively. For the regression of TD onto age, the p-value was 0.00018; this is an evaluation of significance of the regression versus a constant model. In other words, this p-value describes the probability that the data lacked any trend or the probability that the TD does not change with age. The p-value of the regression of THR on age was 0.00294. Overall, these data indicate that there is a significant trend associated with age for both parameters. It should be noted that the Bonferroni correction was applied to both p-values presented in this section to account for the fact that significance testing was performed on a total of four parameters (TD, THR, and two others not reported in this manuscript) obtained from the same data. In addition, we emphasize that the work presented here is intended to be a preliminary exploration of the signals and their potential relationship with arterial physiology. Our goal is to demonstrate correlations that lay the ground work for future experiments.

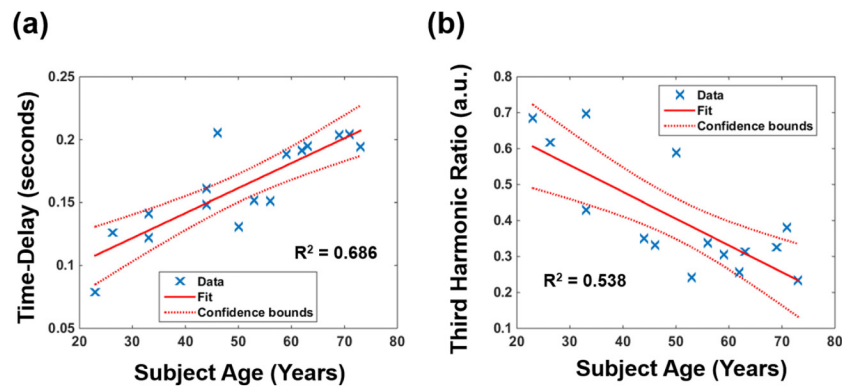**(a)**   **(b)**

Fig. 9. SPG-PPG parameters vs. age. (a) Linear regression of TD onto age. (b) Linear regression of THR onto age. The solid red line is the linear best fit of the data. The curved dotted red lines are the 95% confidence intervals. The blue tick marks indicate the individual data points.

3.4 Cold pressor and exercise challenges

Figure 10 presents SPG-PPG data obtained from a 29-year-old healthy male subject undergoing cold pressor and exercise challenges. Figure 10(a) contains a dual-axis plot of the SPG (blue) and PPG (red) waveforms during 5 seconds of a 2-minute baseline measurement. Figure 10(b) contains a 5-second interval of the cold pressor challenge. Compared with the baseline condition in Fig. 10(a), the PPG waveform in this example is more rounded and contains a steeper systolic upshot. This observation potentially explains why TD is increased in the cold condition. It is also noteworthy that systolic upshot the SPG-signal (blue) in Fig. 10(b) retains its steep slope.

(a)   **(b)**   **(c)**
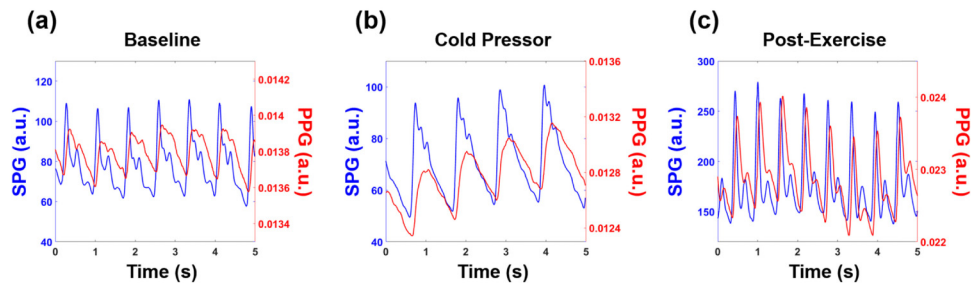

Fig. 10. SPG and PPG signals from each of the physiological challenges. (a) Baseline data. (b) Cold pressor data. (c) Post-exercise data. In each panel, the SPG waveform is blue and the PPG waveform is red, both in arbitrary units.

Figure 10(c) shows a five-second interval acquired after 10 minutes of exercise. The post-exercise PPG waveform has a more pronounced and narrow systolic peak and more closely resembles the SPG waveform than the baseline PPG waveform. In contrast, the baseline PPG waveform has a rounded-off plateau region near the apex. Thus, the location of the PPG peak at baseline is subtler and relatively delayed compared to post-exercise.

Figure 11(a) summarizes repeatability testing of TD on a single subject performing exercise and cold pressor challenges. Each box represents seven repetitions/measurements, and each measurement is an average over approximately 60 heartbeats. For the box marked cold, each measurement consists of average TD at baseline subtracted from average TD during cold-shock (TD cold – TD baseline). Similarly, the box marked exercise contains measurements of baseline subtracted from post-exercise (TD post-exercise – TD baseline). Finally, the box marked baseline is derived from two sequential baseline measurements – one

subtracted from the other (TD baseline 1 – TD baseline 2). This was done to emphasize sensitivity to dynamic changes associated with cold and exercise, and to minimize variability in TD among different measurements. The average increase in TD for the cold challenge was found to be 0.044 seconds, with a range of 0.031 to 0.068 seconds. The average change in TD post-exercise was −0.0578 seconds, with a range of - 0.0110 to - 0.1334 seconds. Notably, the differences between each pair of the three distributions (i.e., cold, exercise and baseline) are statistically significant according to Student's t-test. The p-value for the difference between the cold and exercise distributions is 0.0013, the p-value for the difference between cold and baseline distributions is 0.0031, and the p-value for the difference between exercise and baseline distributions was 0.0286.
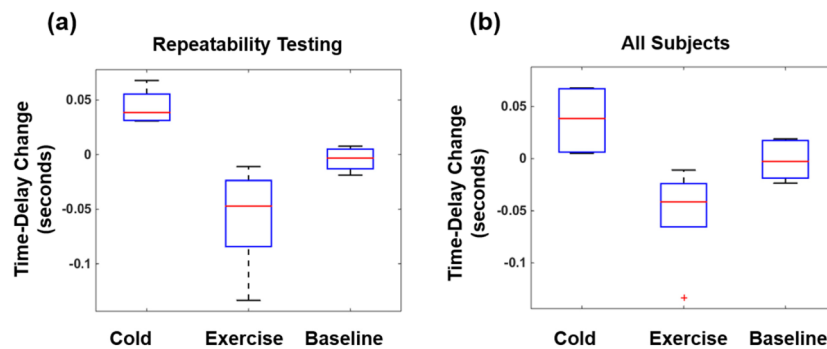

Fig. 11. Changes from baseline in the cold-pressor and exercise challenges. (a) Repeatability testing on a single subject performing seven tandem measurements. Each box plot depicts the range of changes during the cold pressor, exercise and baseline conditions. (b) Changes from baseline obtained from individual measurements performed on four subjects.

Figure 11(b) summarizes the results from four subjects performing the exercise and cold-pressor challenges. As in Fig. 11(a), each box shows how TD changes from baseline for each of the challenge among the individuals. As before, the box labeled "baseline" is the difference between paired 2-minute baseline measurements. The average increase in TD for the cold challenge was found to be 0.0294 seconds, with a range of 0.0051 to 0.0671 second. The average decrease in TD for the exercise challenge was found to be 0.0430 seconds, with a range of 0.0238 to 0.0654 seconds.

4. Discussion

This work introduces methods for extracting physiological parameters from the SPG-PPG signal obtained with ATSA. We demonstrate how the dual SPG-PPG signal is derived from the same raw data obtained with an instrument consisting of a CMOS camera and coherent light source with the SPG originating from flow pulsatility and the PPG originating from volumetric pulsatility. We demonstrate that both waveforms are offset in time and introduce an algorithm characterizing time delay between the systolic peaks. Additionally, we introduce a framework for analyzing SPG structure by calculating harmonic content on a pulse-by-pulse basis. Two signal decomposition methods (time delay and harmonic content) are applied to *in vivo* measurements to demonstrate physiological significance, with our analysis revealing age correlations for both. We proceed to demonstrate changes in time delay associated with exercise (decreased time delay) and cold pressor challenges (increased time delay).

The correlation between age and extracted SPG-PPG parameters suggest that these methods are sensitive to arterial stiffness and vascular aging. Aging arteries undergo mechanical changes resulting in decreased compliance, referred to as arterial stiffening. Thus, the correlations between SPG-PPG signal parameters and age indicate potential sensitivity to these mechanical changes. This implies the methods introduced in this work may be used for noninvasive vascular assessment at early ages as a predictive measure of arterial health

outcomes. We observe that the age-related time delay increases are due to pulse-shape changes in the PPG signal caused by decreased arterial compliance. In fact, these changes in PPG signal shape have been previously observed in the field and reported as an increase in crest time [1, 64]. Our work presents this phenomenon in a new light using the SPG waveform as the reference signal, rather than relying on the PPG waveform which is often subject to artifacts and low signal to noise ratio (Fig. 6) [65, 66]. The mechanism for changes in SPG signal and harmonic content comes from a distinct aspect of vascular physiology. Refractive index mismatch at vessel bifurcations increases with atherosclerosis [67]. This results in the reflection of high-frequency harmonic components as the pulse propagates down the arterial network explaining why there is less harmonic content seen in the older individuals. Our analysis methods could potentiate a noninvasive means of characterizing vascular age for cardiovascular risk stratification. Additionally, it could be applied to early detection of atherosclerosis for early medical and lifestyle interventions.

In this work, harmonic content was characterized using THR rather than other harmonic ratios for two main reasons. First, preliminary analysis demonstrated THR magnitude corresponds with the amount of pulsatile structure; if there are numerous or prominent secondary reflections then THR tends to be larger. Second, the regression of THR onto subject age showed a much stronger correlation than other harmonic ratios. Because of these characteristics, THR was used exclusively in this work to interrogate harmonic content.

The changes in TD caused by cold pressor and exercise challenges indicate a completely different functionality related to vascular tone. Decreased temperature enhances vascular tone to preserve thermal homeostasis by retaining heat in the body's core, whereas increased temperature decreases vascular tone to shed excess heat in peripheral circulation. Overall, the changes in time delay observed in the post-exercise and cold pressor conditions demonstrate that this parameter is sensitive to vascular tone. This is particularly important because vascular resistance is a confounding factor in calculating blood pressure, cardiac output and fluid status [68] meaning that this technique could provide solutions for these medical applications.

This study only partially elucidates the implications of information embedded in the dual SPG-PPG signal. The cardiac pulse is progressively modified by mechanical properties of the underlying vasculature as it propagates down the arterial network. As light transmitted from a single coherent source interacts with the tissue, the pulsatile characteristics of the underlying cardiovascular system are ultimately contained in the SPG-PPG signal. We only present two ways of processing these signals, but there are many other methods that have not yet been explored. Examples include analyzing systolic upstroke time, dicrotic notch prominence, and other harmonic content ratios. Further, almost every processing technique applied to PPG alone could be applied to this new framework. The SPG-PPG signal therefore constitutes a promising technology for continued research.

Overall, this study provides initial data to support the potential clinical significance of the SPG-PPG waveform. The SPG is distinct and possibly more robust than the PPG alone, as shown by the fact that the PPG waveform becomes weak and distorted with vascular constriction, while under these conditions the SPG signal retains its strength and pulsatility (Fig. 6). This may be important because medical applications such as non-invasive cardiac output monitoring have failed due to issues with the PPG signal quality. We have also shown that the SPG and PPG signals provide different and complementary information, specifically flow speed pulsatility from the SPG and vascular expansion pulsatility from the PPG signal. The TD and pulse-shape characteristics of the SPG and PPG waveforms are evidence that they provide unique information, which is further supported by their differential response to contrasting physiological challenges. We conclude that wearable, affixed transmission LSI sensors can generate highly complementary SPG and PPG signals. They potentially provide a single, non-invasive platform for assessing vascular dynamics. Because of their relative

simplicity and ease-of-use, ATSA devices may create new possibilities for non-invasive diagnostics and therapeutic guidance in circulatory diseases.

Disclosures

MG: University of California, Irvine (P), TBR: LAS Inc. (I, E, P), BY: LAS Inc. (I, E, P), SMW: LAS Inc. (I, E, P), BJT University of California, Irvine (P).